Effect of edge plasmons on the optical properties of MoS_2 monolayer flakes

Rossi, Tuomas P.; Winther, Kirsten Trøstrup; Jacobsen, Karsten Wedel; Nieminen, Risto M.; Puska, Martti J.; Thygesen, Kristian Sommer

Published in:
Physical Review B

Link to article, DOI:
10.1103/PhysRevB.96.155407

Publication date:
2017

Document Version
Publisher's PDF, also known as Version of record

PHYSICAL REVIEW B **96**, 155407 (2017)

Effect of edge plasmons on the optical properties of MoS_2 monolayer flakes

Tuomas P. Rossi,[1,*] Kirsten T. Winther,[2] Karsten W. Jacobsen,[2] Risto M. Nieminen,[1]
Martti J. Puska,[1] and Kristian S. Thygesen[2,3,†]

[1]*COMP Centre of Excellence, Department of Applied Physics, Aalto University, P.O. Box 11100, FI-00076 Aalto, Finland*

[2]*CAMD, Department of Physics, Technical University of Denmark, DK-2800 Kgs. Lyngby, Denmark*

[3]*Center for Nanostructured Graphene (CNG), Technical University of Denmark, DK-2800 Kgs. Lyngby, Denmark*

(Received 9 June 2017; revised manuscript received 15 September 2017; published 5 October 2017)

Finite MoS_2 nanoparticles are known to support metallic edge states that are responsible for their catalytic activity. In this work we employ time-dependent density-functional theory (TDDFT) to study the influence of such edge states on the optical properties of triangular MoS_2 monolayer flakes. We find that the edge states support collective plasmon-like excitations that couple strongly to the optical field leading to pronounced absorption peaks below the onset of interband transitions on the basal plane. Additionally, structural relaxation of the flakes can significantly distort the edge states. Thus, we observe that while an evenly-spaced edge configuration supports one-dimensional (1D) plasmon modes similar to those of an ideal 1D electron gas, the relaxed structures show mixed plasmon and single-electron excitations in the low-energy response. Our findings illustrate the sensitivity of the optical response of MoS_2 nanostructures to the details of the edge configuration.

DOI: 10.1103/PhysRevB.96.155407

I. INTRODUCTION

Atomically thin two-dimensional (2D) semiconductors are currently being actively studied due to their unique electronic and optical properties [1,2]. In particular the transition metal dichalcogenides with the chemical formula MX_2 (M: Mo or W; X: S, Se, or Te) have been shown to undergo an indirect to direct band gap transition when the layered bulk materials are thinned down to a single monolayer [3,4]. The monolayers interact strongly with light [5], and the possibility to modify their electronic properties via mechanical strain, electric fields, or van der Waals heterostructuring [6–8] makes the 2D materials a unique platform for controlling light-matter interactions at the atomic length scale.

In a different context, MoS_2 nanoparticles are of interest as nonprecious catalysts for hydrodesulphurization of crude oil products [9] and as electrocatalysts for the hydrogen evolution reaction [10]. It is understood that the edges of the MoS_2 nanoclusters are catalytically active [11–13] and that this is due to the existence of metallic states present at certain edge configurations [14–18]. It has recently been shown that these states can lead to the formation of plasmons, i.e., quantized oscillations of electron gas plasma, along the edges of infinite MoS_2 nanoribbons [19]. This suggests that localized plasmon resonances could form at the edges of finite MoS_2 flakes. The existence of such plasmon resonances could strongly influence the optical properties of the flakes and could potentially be of interest for plasmonic photocatalysis where hot electrons generated by the decay of plasmons are used to drive chemical reactions [20,21]. We note in passing that the plasmons in MoS_2 flakes have recently been studied by means of low-loss electron energy loss spectroscopy [22].

In this paper, we report a detailed computational study of the optical properties of Mo-terminated triangular MoS_2 monolayer nanoflakes with S_2-saturated edges, using time-dependent density-functional theory (TDDFT) [23,24]. This edge configuration is particularly interesting because the metallic edge state on the S_2 dimers supports a strong 1D edge plasmon [19]. Depending on the growth conditions, the flakes favor different edge terminations or shapes [16,25–27]. However, for alternative S-terminated edges, the 1D plasmons are expected to couple weaker to light [19] and they have not been reported in previous computational studies of S-terminated triangular flakes [28,29].

We find that the optical response of the MoS_2 monolayer flakes differs substantially from that of an infinite monolayer. In particular, the absorption spectrum has multiple size-dependent resonances below the absorption onset of the monolayer. Additionally, we find that the optical response is sensitive to the details of the edge geometry. In fact, the structural relaxation of the flakes distorts the edge states, which leads to mixed plasmon and single-electron excitations in the low-energy response. In contrast, an evenly-spaced edge configuration supports 1D edge plasmon resonances.

We analyze the character of the low-energy resonances in detail from the quantum-mechanical Kohn-Sham (KS) density-functional theory (DFT) [30,31] perspective. Specifically, we study the composition of the low-energy resonances in terms of the underlying KS electron-hole transition contributions [32,33]. This analysis shows that the 1D edge plasmons are similar to those of a confined 1D electron gas (1DEG) [34–37], accompanied with screening from the central part of the flake.

The structure of the paper is as follows. In Sec. II, the used computational methods are outlined, and the studied MoS_2 flakes are described in Sec. III. The results (Sec. IV) are divided in subsections. First, we discuss the trends and overall features in the optical response of the flakes of increasing size. Then, we analyze the low-energy resonances and their

*tuomas.rossi@alumni.aalto.fi
†thygesen@fysik.dtu.dk

character in detail. The work is concluded with discussion in Sec. V.

II. METHODS

A. Time-dependent density-functional theory

In DFT, the ground state of the system is obtained from a self-consistent solution of the Kohn-Sham equation

$$H_{\mathrm{KS}}^{(0)}\psi_n^{(0)}(\boldsymbol{r}) = \epsilon_n\psi_n^{(0)}(\boldsymbol{r}), \tag{1}$$

where $H_{\mathrm{KS}}^{(0)}$ is the KS Hamiltonian, $\psi_n^{(0)}(\boldsymbol{r})$ is the nth KS wave function, and ϵ_n the associated eigenvalue. The ground-state wave functions $\psi_n^{(0)}(\boldsymbol{r})$ are chosen to be real-valued functions.

For the response calculation, we use the real-time-propagation TDDFT (RT-TDDFT) method with a δ-pulse perturbation [38]. In this approach, the time-dependent Kohn-Sham equation,

$$i\frac{\partial}{\partial t}\psi_n(\boldsymbol{r},t) = H_{\mathrm{KS}}(t)\psi_n(\boldsymbol{r},t), \tag{2}$$

is propagated in discretized time steps with the initial state given by the ground state, i.e., $\psi_n(\boldsymbol{r},t=0) = \psi_n^{(0)}(\boldsymbol{r})$. The time-dependent Hamiltonian contains a δ-pulse perturbation of form

$$H_{\mathrm{KS}}(t) = H_{\mathrm{KS}}^{(0)} + xK\delta(t) \tag{3}$$

describing the interaction with external electromagnetic radiation within the dipole approximation. In Eq. (3), the electric field is assumed to be aligned along the x direction and the constant K is proportional to the external electric field strength, which is assumed to be small enough to induce only negligible nonlinear effects. During the propagation, the quantities of interest are recorded, and as a post-processing step the time-domain quantities can be Fourier transformed into the frequency domain [see Eq. (5) in the next section].

B. Kohn-Sham decomposition analysis

We analyze the response of the MoS_2 flakes by using a recently implemented Kohn-Sham decomposition tool [33]. This analysis is based on the time-dependent KS density matrix expressed in the KS electron-hole (eh) basis

$$\rho_{ia}^x(t) = \sum_n \left\langle\psi_i^{(0)}\middle|\psi_n(t)\right\rangle f_n \left\langle\psi_n(t)\middle|\psi_a^{(0)}\right\rangle, \tag{4}$$

where f_n is the occupation factor of the nth KS state, and the indices i and a are associated to occupied and unoccupied KS states, respectively. Here the superscript x reminds that the time evolution of the density matrix is calculated for a specific perturbation [see Eq. (3)]. The real part of the density matrix, $\mathrm{Re}[\rho_{ia}^x(t)]$, can be used for accessing observables based on the density, and its linear response in the frequency space is given by the Fourier transform

$$\delta\rho_{ia}^x(\omega) = \frac{1}{K}\int_0^T \mathrm{Re}\left[\rho_{ia}^x(t) - \rho_{ia}(0^-)\right]e^{i\omega t}e^{-\sigma^2t^2/2}\mathrm{d}t, \tag{5}$$

where T is the total propagation time. The Gaussian function $e^{-\sigma^2t^2/2}$ in Eq. (5) ensures that the signal is damped at $t = T$ and leads to Gaussian line shapes for excitations in the frequency space, modeling, e.g., the finite lifetime of the excitations and instrumental broadening. Alternatively, the Lorentzian line shape could be obtained by using an exponential decay function $e^{-\eta t}$ instead of the Gaussian function in Eq. (5).

The linear-response density matrix $\delta\rho_{ia}^x(\omega)$ gives access to other relevant quantities, such as the induced electron density,

$$\delta n_x(\boldsymbol{r},\omega) = 2\sum_{ia}^{\mathrm{eh}} \psi_i^{(0)}(\boldsymbol{r})\psi_a^{(0)}(\boldsymbol{r})\delta\rho_{ia}^x(\omega), \tag{6}$$

and the photoabsorption described by the dipole strength function,

$$S_x(\omega) = -\frac{4\omega}{\pi}\sum_{ia}^{\mathrm{eh}} \mu_{ia}^x \mathrm{Im}\left[\delta\rho_{ia}^x(\omega)\right], \tag{7}$$

where the summations are over the occupied (i) and unoccupied (a) KS states, and $\mu_{ia}^x = \langle i|x|a\rangle$ is the dipole matrix element (see Ref. [33] for details).

In this paper, we first identify the optical resonances of the system by considering the photoabsorption spectrum and then analyze their resonant KS electron-hole contributions as given by $\mathrm{Im}[\delta\rho_{ia}^x(\omega)]$. However, the sign (negative or positive) of $\mathrm{Im}[\delta\rho_{ia}^x(\omega)]$ depends on the signs of the real-valued $\psi_i^{(0)}$ and $\psi_a^{(0)}$ (or on their phase factors in general). Here, we fix the sign convention to the sign of the transition dipole moment μ_{ia}^x, that is, we analyze the transition contributions as given by the weight

$$w_{ia}(\omega) = 2\,\mathrm{sgn}\left(\mu_{ia}^x\right)\mathrm{Im}\left[\delta\rho_{ia}^x(\omega)\right] = 2\,\frac{\mu_{ia}^x}{\left|\mu_{ia}^x\right|}\,\mathrm{Im}\left[\delta\rho_{ia}^x(\omega)\right]. \tag{8}$$

With this convention, the sign of $w_{ia}(\omega)$ reflects the sign of the photoabsorption contribution [see Eq. (7) and Ref. [33]], but the magnitude of $w_{ia}(\omega)$ is not affected by the transition dipole moment μ_{ia}^x. This allows us to observe in better detail those KS transitions that have weak dipole contributions, which is advantageous for analyzing the excitations that are not dominantly of dipole character (see, e.g., the discussion on the coupled quadrupole resonance in Sec. IV B).

The transition contribution weight $w_{ia}(\omega)$ is conveniently visualized as a transition contribution map (TCM) [32]. TCM shows the KS electron-hole weight at a chosen ω on a two-dimensional (2D) $(\varepsilon_{\mathrm{o}},\varepsilon_{\mathrm{u}})$ plane spanned by the energy axes for occupied and unoccupied states. To be specific, TCM is given by

$$M_\omega^{\mathrm{TCM}}(\varepsilon_{\mathrm{o}},\varepsilon_{\mathrm{u}}) = \sum_{ia} w_{ia}(\omega)\, g_{ia}(\varepsilon_{\mathrm{o}},\varepsilon_{\mathrm{u}}), \tag{9}$$

where the discrete $i \to a$ transition contributions are broadened by the 2D Gaussian function $g_{ia}(\varepsilon_{\mathrm{o}},\varepsilon_{\mathrm{u}}) = 1/2\pi\sigma^2 \cdot \exp[-[(\varepsilon_{\mathrm{o}}-\epsilon_i)^2 + (\varepsilon_{\mathrm{u}}-\epsilon_a)^2]/2\sigma^2]$ for presenting them on the continuous $(\varepsilon_{\mathrm{o}},\varepsilon_{\mathrm{u}})$ plane. The axes of TCM are augmented with the density of states (DOS) plots corresponding to the occupied and unoccupied DOSes. We apply $\sigma = 0.04$ eV to TCMs and DOSes, corresponding to the full width at half maximum (FWHM) of 94 meV.

We also consider projected TCMs and DOSes. The projections are done based on the LCAO coefficients $C_{\mu n}^{(0)}$ [see

Eq. (10) in the next section]. The coefficients are used to obtain projections to the chosen set atoms, e.g., to the edge atoms, in which case the projection weight p_n of the nth KS state is given by $p_n = \sum_{\mu\in\mathcal{A}} |C^{(0)}_{\mu n}|^2 / \sum_{\mu} |C^{(0)}_{\mu n}|^2$, where $\mathcal{A}$ is the set of atoms on the edge. Then, the weight used in the projected TCM is $w^{\rm proj}_{ia}(\omega) = p_i\, p_a\, w_{ia}(\omega)$.

C. Computational parameters

We perform calculations with the free GPAW code package [39–41] employing the projector augmented-wave (PAW) method [42]. Specifically, we use the RT-TDDFT implementation [43] based on the linear combination of atomic orbitals (LCAO) representation for wave functions [44].

In the LCAO method, the wave function $\psi_n(\boldsymbol{r},t)$ is expanded in local basis functions $\phi_\mu(\boldsymbol{r})$ centered at atomic coordinates

$$\psi_n(\boldsymbol{r},t) = \sum_\mu \phi_\mu(\boldsymbol{r}) C_{\mu n}(t), \tag{10}$$

where $C_{\mu n}(t)$ are the expansion coefficients. We use the default double-ζ polarized (dzp) basis sets for describing the wave functions [44]. We found that these basis sets yield an accurate description of the response by a comparison against the response calculated with the RT-TDDFT implementation [45] using the real-space-grid representation for wave functions (see Appendix for comparison and further discussion). The electrons in the $4d5s$ and $3s3p$ states of Mo and S atoms, respectively, are explicitly included in the calculations, and the remaining electrons are treated as a frozen core within the PAW framework. All the PAW setups and basis sets are generated using the default parameters in GPAW.

For calculating the response of the MoS_2 flakes, we employ the orbital-dependent Gritsenko-van Leeuwen-van Lenthe-Baerends [46] exchange-correlation (xc) potential with the solid-state modification by Kuisma *et al.* (GLLB-SC) [47]. The occupations of the Kohn-Sham electron states are smeared with a Fermi-Dirac distribution with $k_B T = 0.1$ eV to facilitate the convergence with the used xc potential.

The electron density and potentials are presented on a real-space grid with grid spacing 0.3 Å, and the system is surrounded by a vacuum region of at least 6 Å. In order to evaluate the Hartree potential reliably in the response calculations, we have extended the Poisson equation solver in GPAW. The potential is first solved in a very large and coarse grid (in the present case $307 \times 307 \times 154$ Å^3 cell with spacing of 1.2 Å) with the standard multigrid solver. The large cell captures the slowly-decaying tail of the potential created by dipolar charge oscillations excited by the perturbing potential [Eq. (3)]. The obtained coarse potential is used to correct the boundary condition for the Poisson equation on a finer cell covering only a small central part of the initial large cell. Such refinement is performed consecutively until the original fine grid is reached. The advantage of the approach is that it allows us to calculate the slowly-decaying tail of the potential in an efficient manner. In the present case, the used large grid leads to at least 120 Å vacuum around the MoS_2 flakes.

The time propagation is performed in time steps of 20 attoseconds until the total propagation time $T = 30$ femtoseconds is reached. In all the Fourier transforms to the frequency space [see Eq. (5)], we use the Gaussian broadening with $\sigma = 0.08$ eV (FWHM of 190 meV).

As an illustration of the computational cost of the used methodology, the full time-propagation run with the above-described parameters can be calculated in 18 hours by using 144 cores for the MoS_2 flake of side length of $M = 16$ S_2 dimers ($Mo_{136}S_{336}$, 2832 valence electrons; see Sec. III) [48].

In Sec. IV B, a sodium atom chain is used as a reference. Its response is calculated in the Casida formalism [49] with the Perdew-Burke-Ernzerhof (PBE) [50] xc functional and a double-ζ basis set including diffuse unoccupied $3p$ atomic orbital [43] (only the valence electrons originating from the outermost $3s$ electron states of Na atoms are explicitly included in the calculation).

III. MODELS

We consider triangular MoS_2 flakes that have been cut from a monolayer of MoS_2 (lattice constant 3.18 Å and thickness 3.19 Å). The flakes are terminated with Mo atoms and each Mo atom is saturated with a S_2 dimer. We have relaxed the atomic coordinates with the Broyden-Fletcher-Goldfarb-Shanno (BFGS) energy minimization algorithm as implemented in the free ASE package [51,52]. The minimization uses energies and forces calculated with DFT using the PBE [50] xc functional. The computational parameters are similar to those used in the response calculations (see Sec. II C), except a finer grid spacing of 0.2 Å is used and the Hartree potential is solved on the ordinary calculation cell. The D_{3h} symmetry of the flake was enforced during the relaxation. The flake geometry was initialized by setting the edge S_2 dimers in a configuration resembling the corresponding edge of a MoS_2 ribbon [19] and then distorting the S_2 edge without breaking the D_{3h} symmetry. Then, the system was relaxed until the atomic forces were converged to less than 0.02 eV/Å.

The relaxation affects the overall structure of the MoS_2 flake especially in the corners, but most importantly, the relaxation leads to an uneven distribution of S_2 dimers on the edges of the flake. This feature seems to be in agreement with earlier calculations [12,13,26] and possibly with the scanning-tunneling-microscope images of MoS_2 triangles exhibiting a period of two along the Mo edges [12,15,27]. The resulting structure and the corresponding S_2−S_2 distances are shown in Fig. 1. The changes in the edge configuration affect the delocalized electron states on the edge and leads to significant changes in the optical response (see the next section).

In order to have a tractable MoS_2 reference for analyzing the optical properties, we consider an "ideal" MoS_2 flake with an evenly-spaced edge configuration. The ideal structure is cut directly from the MoS_2 monolayer, but the S atoms forming the S_2 edge have been displaced closer to each other so that the edge configuration resembles that of an infinite MoS_2 nanoribbon [19]. This S_2-edge configuration is similar to the relaxed one in Fig. 1 with the exception that the S_2 dimers are distributed evenly along the edge [see Fig. 1(b)].

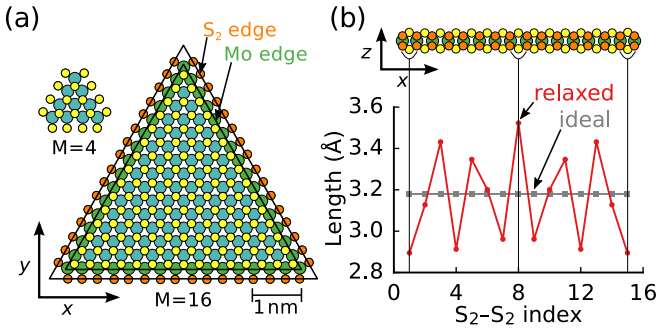

FIG. 1. (a) Top view of the relaxed MoS_2 flakes of side lengths of $M = 4$ and $M = 16$ S_2 dimers. S_2 and Mo edge atoms are marked with different colors. (b) Side view of the $M = 16$ flake and the S_2–S_2 distances of the S_2 dimers on the edge. The relaxation leads to similar uneven S_2-edge configuration in smaller flakes also (see Sec. S1.1 in Supplemental Material) [53].

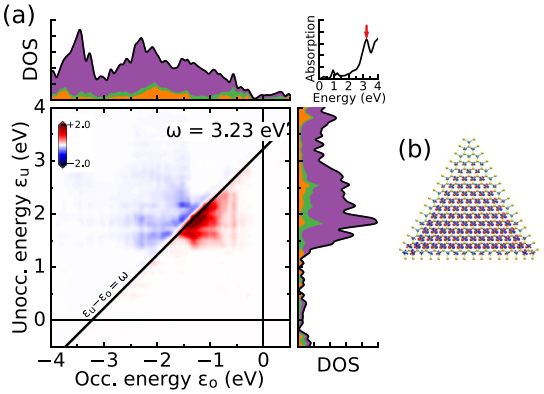

FIG. 3. Analysis of the 3.23 eV resonance of the relaxed $M = 16$ MoS_2 flake. (a) Transition contribution map [Eq. (9)] at 3.23 eV. The axes determine the eigenvalues of the occupied and unoccupied KS states. The Fermi level is at 0 eV. The red and blue colors on the map correspond to positive and negative KS transition contributions [Eq. (8)], respectively, and the color intensity represents the magnitude of the contributions. DOS is decomposed as in Fig. 2(c). (b) Imaginary part of the induced density at 3.23 eV as in the inset of Fig. 2(a).

IV. RESULTS

A. Size-dependent trends in the optical response

We have calculated the optical response of the flakes with the side length ranging from $M = 4$ to $M = 16$, measured as a number of S_2 dimers on each edge. Due to the D_{3h} symmetry of the flake, the photoabsorption spectrum has the symmetry $S_x(\omega) = S_y(\omega)$ on the plane of the flake (xy plane). However, despite this symmetry, the local features in the response (visible in the induced electron density) depend on the orientation of the perturbation. Here, we consider the electric field perturbation aligned along one of the edges of the flake (x direction). Such a perturbation could be realized by an electromagnetic field propagating perpendicularly to the plane of the flake.

The calculated in-plane photoabsorption spectra of the relaxed MoS_2 flakes are shown in Fig. 2(a). The spectra consist of discrete low-energy (<2 eV) peaks and broad absorption at higher energies. As the flake size is increased, the spectrum starts to resemble that of the infinite monolayer with the exception that the low-energy peaks remain below the absorption onset of the monolayer. The low-energy peaks show a general redshifting trend as the flake size is increased, analogously to the low-energy peaks in S-terminated MoS_2 flakes [28]. However, the number of peaks and their intensities show varying trend as the size is increased. The induced electron densities of the low-energy peaks have a substantial contribution from the edge analogously to S-terminated MoS_2 flakes [28]. In contrast, the main contribution to the prominent 3.23 eV excitation originates from the central region of the flake, in agreement with its coincidence with the absorption peak of the infinite monolayer.

For the 3.23 eV resonance, we show in Fig. 3(a) the TCM analysis (see Sec. II B). In agreement with the induced density [Fig. 3(b)], the TCM shows that the resonance is built up from a vast number of transitions localized mostly in the central part of the flake (see the DOS decomposition). The most positive contribution (red areas) originates from transitions relatively close to the resonance energy ω, reflecting the single-particle

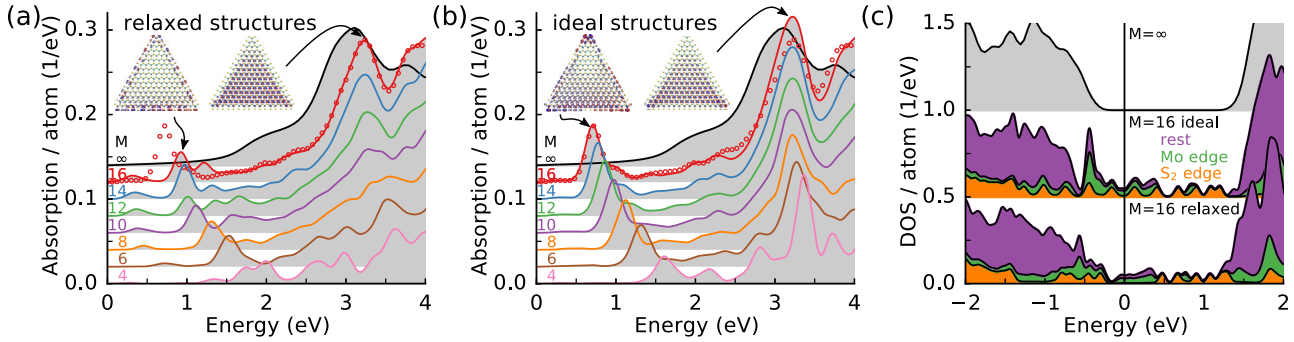

FIG. 2. In-plane photoabsorption spectra of (a) relaxed and (b) ideal MoS_2 monolayer flakes of sizes from $M = 4$ to $M = 16$. Insets show the imaginary parts of the induced electron densities at the marked resonances (red and blue colors correspond to the positive and negative 10% isosurfaces, respectively). The hollow markers show the spectrum of $M = 16$ flake with a relaxed interior but an ideal S_2 edge. (c) Densities of states (DOS) with respect to the Fermi level. Each DOS is decomposed into three contributions (see Fig. 1): S_2 edge (orange; bottom), Mo edge (green; middle), and the other atoms (purple; top). The $M = \infty$ spectra show the absorption (in arb. units) and DOS (with the Fermi level aligned with that of the flakes) of an infinite MoS_2 monolayer [54,55].

character of the resonance [37]. However, some contribution comes also from transitions below ω, indicating that coupling is present among the contributing transitions. We observe also negative contributions (blue areas) from transitions above the resonance frequency, reducing the intensity of the resonance.

In order to understand the origin of the low-energy peaks better, we compare the spectra of relaxed flakes to those of ideal MoS_2 flakes (see Sec. III). The absorption spectra of the ideal flakes are shown in Fig. 2(b). Analogously to the relaxed structures, the ideal flakes exhibit a strong resonance at 3.2 eV with similar characteristics. In contrast to the complex low-energy response of relaxed flakes, in the ideal flakes the low-energy region is dominated mainly by a single peak. With the increasing side length of the flake, this peak shows a clear redshift from 1.6 eV ($M = 4$) to 0.7 eV ($M = 16$) accompanied with a gradual increase in intensity. Such resonance energy and intensity trends are very similar to those of 1DEG and Na_n atom chains [34–37], hinting that the low-energy resonance would correspond to a 1D plasmon mode excited at the metallic edge of the flake [19]. This is supported by the induced density showing a dipole charge density oscillation over the horizontal edge, in analogy to main longitudinal plasmon mode in Na_n [34–37].

The large differences between the low-energy responses of the relaxed and ideal structures illustrate that the low-energy response is very sensitive to the exact edge configuration. In Figs. 2(a) and 2(b) we also show as hollow markers the spectrum of an additional $M = 16$ structure that is identical to the relaxed structure except that the S_2-edge configuration is evened to be similar to that of the ideal flake. It is interesting to note that above 2 eV, the spectrum of this structure follows closely that of the relaxed flake, but for the low-energy response below 2 eV, the response is similar to its ideal counterpart. This strongly illustrates that the low-energy response is determined by the edge effects. Furthermore, relatively small energies are enough to distort the edge configuration. The above-described reconstruction of the ideal S_2 edge on top of the relaxed flake interior increases the PBE ground-state energy by 20 meV per S atom forming the S_2 edge in comparison to the relaxed structure. This energy difference is of the order of thermal energy at room temperature, $k_B T = 25$ meV at $T = 300$ K. Thus, in actual experimental conditions, the edge configuration and the optical response is likely to vary.

In order to understand the changes caused by different edge configurations, we show in Fig. 2(c) the densities of states of the relaxed and ideal $M = 16$ flakes as well as DOS of an infinite monolayer. Whereas the monolayer has a clear band gap, the finite flakes show expectedly states inside the band gap. The DOS is decomposed into its contributions from the S_2 dimers and Mo atoms on the edge. In the ideal flake, we observe a set of states localized on the S_2 and Mo edges. These states constitute discrete finite-size counterparts of the corresponding 1D electron bands in MoS_2 nanoribbon [compare to the band structure, e.g., in Fig. 2(a) of Ref. [19]]. Due to the symmetry of the flake, the peaks in the S_2-edge DOS originate from three nearly-degenerate KS states. The distortion of the evenly-spaced S_2 edge by the structural relaxation opens a band gap in the corresponding 1D electron band analogously to Peierls distortion of 1D crystal. This is visible in the DOS of the relaxed flake [Fig. 2(c)] as a grouping of S_2-edge-localized states. Importantly, such S_2-edge states are not present near the Fermi level in the relaxed flake.

The differences in the electronic structure cause the major changes in the optical response. In the following two subsections, we analyze its effect on the different low-energy resonances. The main conclusion is that in the ideal flakes the low-energy resonances correspond to the edge plasmons similar to those of 1DEG, whereas in the relaxed flakes the resonances have mainly single-electron character.

B. Ideal flakes: 1D edge plasmons

We focus on the low-energy resonances originating from the S_2 dimers on the edge using the ideal $M = 16$ MoS_2 flake as a prototype. In Fig. 4, we show the S_2-edge-projected TCMs (see Sec. II B) and induced densities of the resonance peaks at 0.71 eV, 1.02 eV, and 1.42 eV. Here, we consider only the projected TCM emphasizing the contribution from the edge. The full TCMs show screening and other contributions by the KS transitions localized in the other parts of the flake (see Sec. S1.2 of Supplemental Material for the full TCMs) [53]. Such contributions are also visible in the full induced densities shown in Figs. 4(a_1)–4(c_1). The KS transitions marked in TCMs [Figs. 4(a)–4(c)] are characteristic for the resonances and their S_2-edge-projected induced density contributions are shown in Figs. 4(a_2)–4(c_2). We also consider a Na_{16} atom chain with a bond length of 3.5 Å as a reference system modeling a confined 1DEG.

For the 0.71 eV resonance, the main positive contributing comes from a few low-energy transitions localized on the S_2 edge [Fig. 4(a); note that the occupation number smearing used in the calculations to facilitate convergence leads also to contributions from fractionally occupied transitions with $\varepsilon_o > 0$ or $\varepsilon_u < 0$ near the Fermi level]. The marked positively contributing transitions lead to dipole charge density oscillation on the edge [Fig. 4(a_2)], which is present in the full induced density also [Fig. 4(a_1)]. The dipole charge density oscillation is clearest along the edge parallel to the electric field direction (horizontal x direction), but also the other two edges show the pattern. This indicates that the interaction between individual edges is relatively weak and, as an approximation, a superposition of the 1D dipole plasmons along all three edges of the flake is observed.

The 0.71 eV excitation of the MoS_2 flake is analogous to the longitudinal dipole plasmon in sodium atom chains [34–37]. Even though such a plasmon mode comprises mostly a single Kohn-Sham transition [57], its resonance energy is much higher than that of the underlying KS transition due to the Coulomb interaction. This is a distinct characteristic of plasmonic excitations [37]. Similar characteristics are also true for the 0.71 eV excitation of the MoS_2 flake (in TCM the diagonal line marking ω is much higher than the contributing transition near the Fermi level). Overall, the S_2-edge-projected TCM is very similar to the TCM of Na_{16} dipole plasmon [inset of Fig. 4(a)]. Thus, we interpret the 0.71 eV resonance as a 1D dipole edge plasmon resonance.

Considering the fainter 1.02 eV resonance, it interestingly corresponds to an antisymmetric combination of 1D quadrupole plasmon modes at the two slanted edges of the

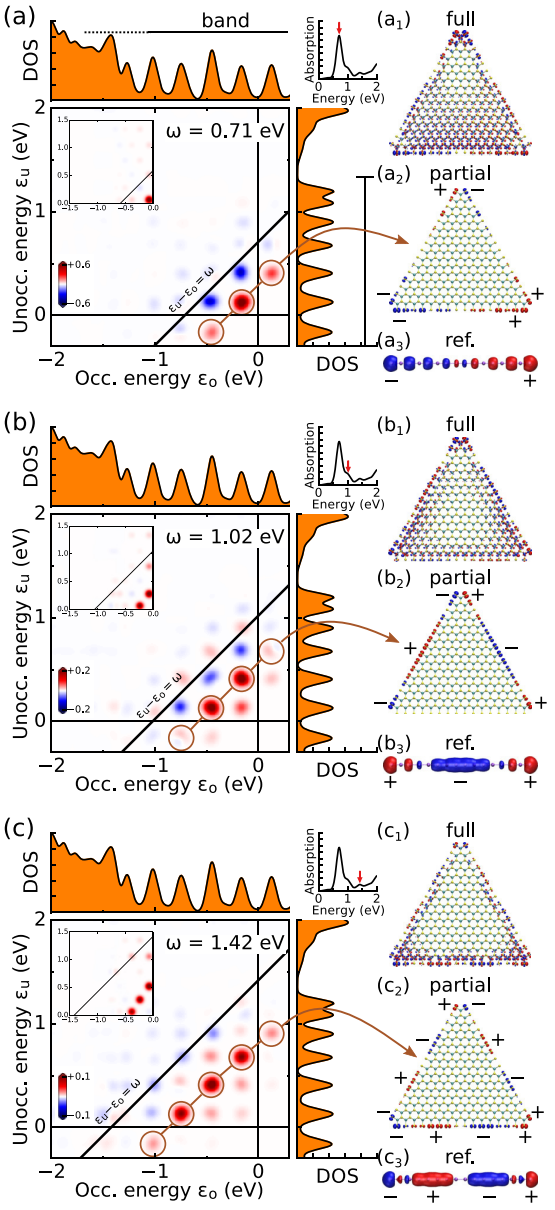

FIG. 4. Analysis of the edge plasmon modes of ideal $M = 16$ flake. S_2-edge-projected TCMs at (a) 0.71 eV, (b) 1.02 eV, and (c) 1.42 eV. DOS show only the contribution from the S_2 edge. TCMs of the corresponding plasmon modes of Na_{16} chain are shown as insets [56]. The subpanels on the right-hand side depict the 10% isosurfaces of the imaginary part of (a_1)–(c_1) the full and (a_2)–(c_2) partial induced densities of the edge plasmon modes, and (a_3)–(c_3) the analogous densities of the Na_{16} chain. The partial induced density corresponds to the contribution from the KS transitions marked in TCMs.

flake [Fig. 4($b_{1,2}$)]. Due to the fact that such an antisymmetric combination is possible in the present triangular geometry, the total response is dipole active and observed in the photoabsorption spectrum. This indicates that the interaction between different edges is not negligible but sufficient to render such coupled quadrupole plasmon modes visible in the spectrum. A similar quadrupole mode can also be found in the sodium atom chain as a dipole-forbidden resonance. The TCMs of the 1.02 eV resonance and the analogous quadrupole mode of Na_{16} [Fig. 4(b)] [56] are again very similar.

Further, at 1.42 eV, we observe a linear octupole edge plasmon mode [Fig. 4($c_{1,2}$)]. This mode is analogous to the dipole mode but it has an increased number of nodes in the charge density pattern. The resonance is similar to the corresponding one in Na_{16}, both in terms of TCM [Fig. 4(c)] and induced density pattern [Fig. 4(c_3)].

The TCMs of the 1D plasmon modes of the considered $M = 16$ MoS_2 flake and those of the Na_{16} chain have a particular difference though. The dipole plasmon mode [Fig. 4(a)] has a negative contribution from the KS transitions that form the quadrupole plasmon mode [Fig. 4(b)]. Similarly, the quadrupole mode has negative contribution from the octupole plasmon transitions [Fig. 4(c)]. While some of this mixing can originate from the used spectral broadening, we expect that the main contribution comes from the interaction between the resonances, allowing the lower-energy plasmon mode to be screened by the higher-energy plasmon mode. In Na_{16}, such interaction is not present because the quadrupole resonance is strictly dipole forbidden [56] and it cannot couple to the dipole and octupole modes. In contrast, the triangular composition of the edges in MoS_2 flakes renders the coupled quadrupole mode dipole active and it is further able to couple to the other plasmon modes. This leads to a more detailed edge response in the full induced density [Figs. 4(a_1)–4(c_1)] in comparison to the intact plasmon mode [Figs. 4(a_2)–4(c_2)].

It is intriguing to consider the trends observed in the TCMs. Both in the $M = 16$ MoS_2 flake and the Na_{16}, the number of (nondegenerate) positively contributing transitions increases by one from the dipole to the quadrupole mode and from the quadrupole to the octupole mode. This can be readily understood as follows. In a confined 1DEG, single-particle wave functions are particle-in-a-box-like, i.e., of the form $\psi_n(x) \sim \sin(n2\pi x/L)$, where L is the length of the box. The first excitation (dipole) corresponds to an excitation from highest occupied molecular orbital (HOMO) to lowest unoccupied molecular orbital (LUMO), i.e., to a change in the quantum number of $\Delta n = 1$. The second excitation (quadrupole) corresponds to a constructive superposition of two transitions HOMO $- 1 \rightarrow$ LUMO and HOMO $\rightarrow$ LUMO $+ 1$, both of which have $\Delta n = 2$ (and no other transitions have $\Delta n = 2$). Similarly, the third excitation (octupole) corresponds to a constructive superposition of the three possible transitions with $\Delta n = 3$. TCMs show that such transitions with a similar nodal character couple strongly together and form the corresponding plasmon mode. In all the cases, analogously to the dipole plasmon mode, the constructively contributing KS transitions are low in energy in comparison to the excitation frequency due to the strong Coulomb coupling (i.e., they lie well below the $\varepsilon_u - \varepsilon_o = \omega$ line), illustrating their plasmonic character [37]. In comparison to infinite 1DEG with a 1D metallic band, the present plasmon modes can be considered as localized counterparts of the extended 1D plasmon with different q vectors.

The low-energy resonances of smaller flakes [Fig. 2(b)] have similar characteristic as described here for the $M = 16$ flake (see Sec. S1.2 in Supplemental Material) [53]. As

a general size effect, the decreasing flake size leads to increasingly prominent quantization of the discrete electron states associated to the same 1D electron "band." The edge length and the order of the plasmon mode can be associated with the wavelength of the plasmon oscillation. As the flake size and the wavelength are decreased, the resonance energy increases [Fig. 2(b)]. This is analogous to the energy–q-vector dispersion of extended 1D plasmon modes [19]. In the smallest $M = 4$ flake, the low-energy resonance at 1.61 eV starts to be close to the onset of the nearly continuum of electron transitions localized in the central parts of the flake.

C. Relaxation: Plasmons vs interband excitations

The relaxed $M = 16$ flake shows three main low-energy resonances at 0.31 eV, 0.92 eV, and 1.21 eV [Fig. 2(a)]. First, we analyze the most intense 0.92 eV and 1.21 eV resonances that originate from the S_2 edge. The S_2-edge-projected TCMs and DOSes are shown in Figs. 5(a) and 5(b). Due to the distortions in the configuration of the edge atoms, the electronic structure of the S_2 edge is greatly different from that of the ideal flake [compare DOSes in Figs. 5(a) and 5(b) to those in Figs. 4(a)–4(c)]. Specifically, the HOMO and LUMO states on the S_2 edge are separated by nearly 0.8 eV, corresponding to an opening of a band gap in the 1D electron band on the S_2 edge [see the "bands" marked in the DOSes of Figs. 4(a) and 5(a)]. Similar increased separation between HOMO and LUMO S_2-edge state is present in the other flake sizes also (see the DOSes in Sec. S1.2 of Supplemental Material) [53]. Such difference causes the S_2-edge-localized resonances to be higher in energy in comparison to the edge plasmons of the ideal flakes discussed in the previous section.

It is interesting to consider how the characters of the S_2-edge resonances change in comparison to the ideal flake. The 0.92 eV resonance [Fig. 5(a)] is mostly a HOMO-LUMO transition like the 0.71 eV dipole plasmon in the ideal flake. However, the coupling strength is smaller, i.e., the resonance energy is closer to the underlying KS single-electron transition energy. In addition, in the 1D electron band picture, this transition would correspond to an interband transition, whereas the dipole plasmon in the ideal flake ideal corresponds to an intraband transition, although both transitions are HOMO-LUMO transitions of the finite flake. The small Coulomb coupling and the interband character of the resonance indicate the single-electron character of the resonance. Despite these remarks, it is interesting to note that the induced density pattern is delocalized over the whole S_2 edge, analogously to the edge plasmon.

The qualitative features of the 1.21 eV resonance are similar to the 0.92 eV resonance. While the induced density shows slightly delocalized oscillation over the edge, the coupling strength appears to be small in comparison to the edge plasmons of the ideal flake, indicating the single-electron character of the transition [37].

At the 1.21 eV resonance, we can also find a contribution from a charge density pattern similar to the quadrupole 1.02 eV plasmon in the ideal flake. This is illustrated by considering the induced density contribution [Fig. 5(b_3)] of the two KS transitions marked in Fig. 5(b). A quadrupole pattern similar to

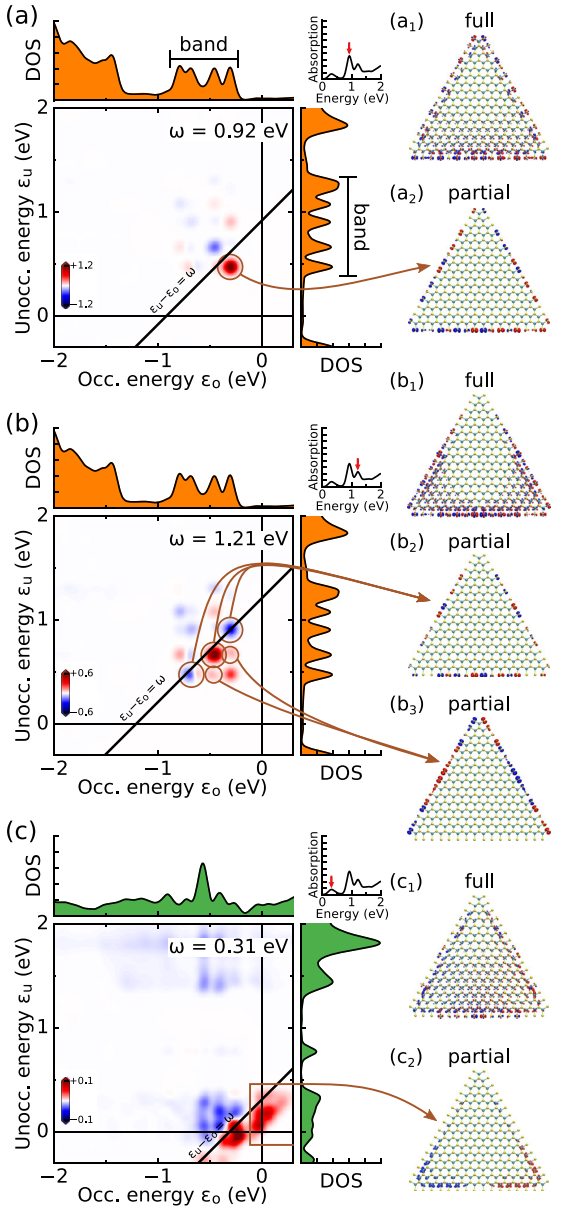

FIG. 5. Analysis of the low-energy resonances of the relaxed $M = 16$ flake. S_2-edge-projected TCMs at (a) 0.92 eV and (b) 1.21 eV, and Mo-edge-projected TCM at (c) 0.31 eV. DOSes show only the corresponding projections. The full and partial induced densities are shown analogously to Fig. 4.

Fig. 4($b_{2,3}$) is observed. These transitions contribute to the total induced density and affect the full induced density patterns [Fig. 5(b_1)] especially along the two edges that are slanted with respect to the horizontal x axis.

By the above analysis, the low-energy 0.92 eV and 1.21 eV resonances seem to be single-electron transitions localized on the edge, though particular similarities to the 1D edge plasmons in ideal flakes can be found. The low-energy resonances of smaller flakes share similar general features (see Sec. S1.2 of Supplemental Material) [53].

Finally, we analyze the lowest 0.31 eV resonance, which is of different character and originates mainly from the Mo edge of the flake. The Mo-edge-projected TCM shown in

Fig. 5(c) reveals that the constructive positive contribution originates from various coupled transitions localized on the Mo edge. We observe nearly a continuum of Mo edge localized states at the Fermi level, and in the 1D electron band picture, the 0.31 eV resonance corresponds to an intraband transition. In fact, the induced density resembles the 1D edge plasmon localized on the Mo edge atoms, which is also observed in MoS_2 nanoribbons [19]. The relaxation does not significantly disturb the configuration of the Mo edge atoms, and correspondingly such a plasmon mode can be observed. Analogous plasmon modes can also be observed in smaller flakes [see Fig. 2(a) and Sec. S1.2 of Supplemental Material for TCMs] [53].

In the ideal flake, the Mo-edge plasmon analogous to the 0.31 eV resonance has a diminishing intensity. We expect this to be due to the interplay between the Mo- and S_2-edge plasmons. In the ideal flakes, the S_2-edge plasmon dominates the low-energy response and screens strongly the lower-lying Mo-edge plasmon and suppresses its intensity. Such a suppression can be observed in the relaxed flake also. Namely, in the full induced density [Fig. 5(c_1)], we observe a counterdipole on the S_2 edge. This screening originates mainly from the same S_2-edge-localized transition that builds up the 0.92 eV resonance (see the full TCM at 0.31 eV in Sec. S1.2.2 of Supplemental Material) [53].

V. CONCLUSIONS

In this paper, we have studied the optical properties of MoS_2 monolayer flakes with S_2-saturated Mo edges. Our calculations suggest that the edge-localized electron states lead to a strong optical response below the absorption onset of the monolayer. Such low-energy resonances were found to be sensitive to the exact edge configuration, and the structural relaxation was found to distort the evenly-spaced S_2 edge.

We analyzed the low-energy resonances in detail in terms of the contributing Kohn-Sham single-electron transitions as well as by considering their full and edge-projected real-space induced density responses. The analyses allowed us to recognize 1D edge plasmons supported by the evenly-spaced S_2 edge. In contrast, the low-energy resonances in the relaxed distorted edge were found to have mainly single-particle character. However, the distortion renders the 1D plasmon localized on the Mo atoms on the edge visible in the absorption spectrum.

It is important to note that the energy required to alter the edge configuration is relatively small. Thus, the experimental conditions such as finite temperature or underlying substrate can dictate the edge structure and, correspondingly, the optical low-energy response. When evenly-spaced edge is present, our work suggests that MoS_2 edges might be suitable for realizing atomically confined 1D plasmons at finite scale [34–37,57–59], complementing experiments on analogous extended 1D plasmons [60–62]. On the other hand, the low-energy response of MoS_2 flakes might be advantageous for photocatalysis [20]. Similar optical properties might also be exhibited by the metallic states on defect lines [63] and domain boundaries [64–66]. All in all, our study emphasizes the rich optical response of MoS_2 nanoflakes, simultaneously illustrating the importance of powerful analysis tools for extracting information on the optical response.

ACKNOWLEDGMENTS

We thank the Academy of Finland for support through its Centres of Excellence Programme (2012–2017) under Projects No. 251748 and No. 284621. The Center for Nanostructured Graphene (CNG) is sponsored by the Danish National Research Foundation, Project No. DNRF103. T.P.R. thanks the Vilho, Yrjö, and Kalle Väisälä Foundation of the Finnish Academy of Science and Letters and the Finnish Cultural Foundation for support. We acknowledge computational resources provided by CSC – IT Center for Science (Finland), the Aalto Science-IT project (Aalto University School of Science), and the Niflheim supercomputer (Technical University of Denmark). The NumPy [67] and Matplotlib [68] Python packages and the VMD software [69,70] were used for processing the data and generating the figures.

APPENDIX : BASIS SET CONVERGENCE

In Fig. 6, we show the photoabsorption spectrum of the ideal $M = 6$ flake calculated with the dzp LCAO basis sets and with the finite-difference real-space grid representation, which essentially corresponds to the complete-basis-set limit. In the finite-difference calculation, the wave functions are represented on a uniform rectangular grid. The grid spacing of 0.3 Å and all the other computational parameters (including the extended Poisson solver, see Sec. II C) are the same as with the LCAO calculation. (The spectra are only minimally affected by decreasing the grid spacing to 0.2 Å, increasing the vacuum size to 8 Å, or decreasing the time step to 10 as.)

The used dzp basis sets yield only a small deviation from the complete-basis-set limit in the considered energy range. This is in contrast to metal nanoparticles, where the default dzp basis sets are insufficient due to the lacking diffuse functions [43,71]. We expect that the reason for the better performance of the dzp basis sets for MoS_2 flakes is that for these structures the diffuse functions are not so important due to minimal spill-out of surface charge in comparison to metal nanoparticles.

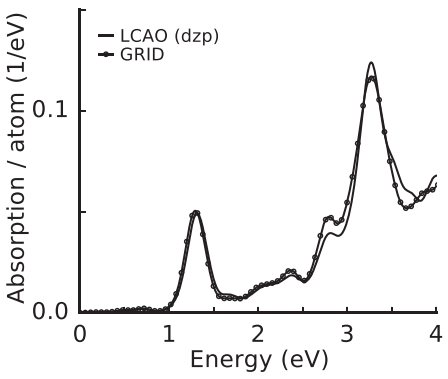

FIG. 6. Photoabsorption spectrum of the ideal $M = 6$ flake calculated with the dzp LCAO basis sets and with the real-space grid representation of the wave functions yielding the complete-basis-set limit.

[1] G. R. Bhimanapati, Z. Lin, V. Meunier, Y. Jung, J. Cha, S. Das, D. Xiao, Y. Son, M. S. Strano, V. R. Cooper, L. Liang, S. G. Louie, E. Ringe, W. Zhou, S. S. Kim, R. R. Naik, B. G. Sumpter, H. Terrones, F. Xia, Y. Wang, J. Zhu, D. Akinwande, N. Alem, J. A. Schuller, R. E. Schaak, M. Terrones, and J. A. Robinson, ACS Nano **9**, 11509 (2015).

[2] A. C. Ferrari, F. Bonaccorso, V. Fal'ko, K. S. Novoselov, S. Roche, P. Boggild, S. Borini, F. H. L. Koppens, V. Palermo, N. Pugno, J. A. Garrido, R. Sordan, A. Bianco, L. Ballerini, M. Prato, E. Lidorikis, J. Kivioja, C. Marinelli, T. Ryhanen, A. Morpurgo, J. N. Coleman, V. Nicolosi, L. Colombo, A. Fert, M. Garcia-Hernandez, A. Bachtold, G. F. Schneider, F. Guinea, C. Dekker, M. Barbone, Z. Sun, C. Galiotis, A. N. Grigorenko, G. Konstantatos, A. Kis, M. Katsnelson, L. Vandersypen, A. Loiseau, V. Morandi, D. Neumaier, E. Treossi, V. Pellegrini, M. Polini, A. Tredicucci, G. M. Williams, B. Hee Hong, J.-H. Ahn, J. Min Kim, H. Zirath, B. J. van Wees, H. van der Zant, L. Occhipinti, A. Di Matteo, I. A. Kinloch, T. Seyller, E. Quesnel, X. Feng, K. Teo, N. Rupesinghe, P. Hakonen, S. R. T. Neil, Q. Tannock, T. Lofwander, and J. Kinaret, Nanoscale **7**, 4598 (2015).

[3] K. F. Mak, C. Lee, J. Hone, J. Shan, and T. F. Heinz, Phys. Rev. Lett. **105**, 136805 (2010).

[4] A. Splendiani, L. Sun, Y. Zhang, T. Li, J. Kim, C.-Y. Chim, G. Galli, and F. Wang, Nano Lett. **10**, 1271 (2010).

[5] F. Withers, O. Del Pozo-Zamudio, A. Mishchenko, A. P. Rooney, A. Gholinia, K. Watanabe, T. Taniguchi, S. J. Haigh, A. K. Geim, A. I. Tartakovskii, and K. S. Novoselov, Nat. Mater. **14**, 301 (2015).

[6] H. J. Conley, B. Wang, J. I. Ziegler, R. F. Haglund, S. T. Pantelides, and K. I. Bolotin, Nano Lett. **13**, 3626 (2013).

[7] F. H. L. Koppens, D. E. Chang, and F. J. García de Abajo, Nano Lett. **11**, 3370 (2011).

[8] A. K. Geim and I. V. Grigorieva, Nature (London) **499**, 419 (2013).

[9] H. Topsøe, B. S. Clausen, and F. E. Massoth, *Hydrotreating Catalysis* (Springer, Berlin, Heidelberg, 1996).

[10] P. C. K. Vesborg, B. Seger, and I. Chorkendorff, J. Phys. Chem. Lett. **6**, 951 (2015).

[11] T. F. Jaramillo, K. P. Jørgensen, J. Bonde, J. H. Nielsen, S. Horch, and I. Chorkendorff, Science **317**, 100 (2007).

[12] A. Bruix, H. G. Füchtbauer, A. K. Tuxen, A. S. Walton, M. Andersen, S. Porsgaard, F. Besenbacher, B. Hammer, and J. V. Lauritsen, ACS Nano **9**, 9322 (2015).

[13] A. Bruix, J. V. Lauritsen, and B. Hammer, Faraday Discuss. **188**, 323 (2016).

[14] S. Helveg, J. V. Lauritsen, E. Lægsgaard, I. Stensgaard, J. K. Nørskov, B. S. Clausen, H. Topsøe, and F. Besenbacher, Phys. Rev. Lett. **84**, 951 (2000).

[15] M. V. Bollinger, J. V. Lauritsen, K. W. Jacobsen, J. K. Nørskov, S. Helveg, and F. Besenbacher, Phys. Rev. Lett. **87**, 196803 (2001).

[16] M. V. Bollinger, K. W. Jacobsen, and J. K. Nørskov, Phys. Rev. B **67**, 085410 (2003).

[17] J. V. Lauritsen, M. Nyberg, R. T. Vang, M. V. Bollinger, B. S. Clausen, H. Topsøe, K. W. Jacobsen, E. Lægsgaard, J. K. Nørskov, and F. Besenbacher, Nanotechnology **14**, 385 (2003).

[18] H. Pan and Y.-W. Zhang, J. Mater. Chem. **22**, 7280 (2012).

[19] K. Andersen, K. W. Jacobsen, and K. S. Thygesen, Phys. Rev. B **90**, 161410 (2014).

[20] S. Linic, U. Aslam, C. Boerigter, and M. Morabito, Nat. Mater. **14**, 567 (2015).

[21] C. Zhang, H. Zhao, L. Zhou, A. E. Schlather, L. Dong, M. J. McClain, D. F. Swearer, P. Nordlander, and N. J. Halas, Nano Lett. **16**, 6677 (2016).

[22] H. C. Nerl, K. T. Winther, F. S. Hage, K. S. Thygesen, L. Houben, C. Backes, J. N. Coleman, Q. M. Ramasse, and V. Nicolosi, npj 2D Mater. Appl. **1**, 2 (2017).

[23] E. Runge and E. K. U. Gross, Phys. Rev. Lett. **52**, 997 (1984).

[24] C. A. Ullrich, *Time-Dependent Density-Functional Theory: Concepts and Applications* (Oxford University Press, New York, 2012).

[25] J. P. Wilcoxon, P. P. Newcomer, and G. A. Samara, J. Appl. Phys. **81**, 7934 (1997).

[26] H. Schweiger, P. Raybaud, G. Kresse, and H. Toulhoat, J. Catal. **207**, 76 (2002).

[27] J. V. Lauritsen, J. Kibsgaard, S. Helveg, H. Topsoe, B. S. Clausen, E. Laegsgaard, and F. Besenbacher, Nat. Nano **2**, 53 (2007).

[28] T. B. Wendumu, G. Seifert, T. Lorenz, J.-O. Joswig, and A. Enyashin, J. Phys. Chem. Lett. **5**, 3636 (2014).

[29] J.-O. Joswig, T. Lorenz, T. B. Wendumu, S. Gemming, and G. Seifert, Acc. Chem. Res. **48**, 48 (2015).

[30] P. Hohenberg and W. Kohn, Phys. Rev. **136**, B864 (1964).

[31] W. Kohn and L. J. Sham, Phys. Rev. **140**, A1133 (1965).

[32] S. Malola, L. Lehtovaara, J. Enkovaara, and H. Häkkinen, ACS Nano **7**, 10263 (2013).

[33] T. P. Rossi, M. Kuisma, M. J. Puska, R. M. Nieminen, and P. Erhart, J. Chem. Theory Comput., doi:10.1021/acs.jctc.7b00589.

[34] S. Gao and Z. Yuan, Phys. Rev. B **72**, 121406 (2005).

[35] J. Yan, Z. Yuan, and S. Gao, Phys. Rev. Lett. **98**, 216602 (2007).

[36] J. Yan and S. Gao, Phys. Rev. B **78**, 235413 (2008).

[37] S. Bernadotte, F. Evers, and C. R. Jacob, J. Phys. Chem. C **117**, 1863 (2013).

[38] K. Yabana and G. F. Bertsch, Phys. Rev. B **54**, 4484 (1996).

[39] J. J. Mortensen, L. B. Hansen, and K. W. Jacobsen, Phys. Rev. B **71**, 035109 (2005).

[40] J. Enkovaara, C. Rostgaard, J. J. Mortensen, J. Chen, M. Duak, L. Ferrighi, J. Gavnholt, C. Glinsvad, V. Haikola, H. A. Hansen, H. H. Kristoffersen, M. Kuisma, A. H. Larsen, L. Lehtovaara, M. Ljungberg, O. Lopez-Acevedo, P. G. Moses, J. Ojanen, T. Olsen, V. Petzold, N. A. Romero, J. Stausholm-Møller, M. Strange, G. A. Tritsaris, M. Vanin, M. Walter, B. Hammer, H. Häkkinen, G. K. H. Madsen, R. M. Nieminen, J. K. Nørskov, M. Puska, T. T. Rantala, J. Schiøtz, K. S. Thygesen, and K. W. Jacobsen, J. Phys.: Condens. Matter **22**, 253202 (2010).

[41] "GPAW: DFT and beyond within the projector-augmented wave method", https://wiki.fysik.dtu.dk/gpaw/ (accessed June 1, 2017).

[42] P. E. Blöchl, Phys. Rev. B **50**, 17953 (1994).

[43] M. Kuisma, A. Sakko, T. P. Rossi, A. H. Larsen, J. Enkovaara, L. Lehtovaara, and T. T. Rantala, Phys. Rev. B **91**, 115431 (2015).

[44] A. H. Larsen, M. Vanin, J. J. Mortensen, K. S. Thygesen, and K. W. Jacobsen, Phys. Rev. B **80**, 195112 (2009).

[45] M. Walter, H. Häkkinen, L. Lehtovaara, M. Puska, J. Enkovaara, C. Rostgaard, and J. J. Mortensen, J. Chem. Phys. **128**, 244101 (2008).

[46] O. Gritsenko, R. van Leeuwen, E. van Lenthe, and E. J. Baerends, Phys. Rev. A **51**, 1944 (1995).
[47] M. Kuisma, J. Ojanen, J. Enkovaara, and T. T. Rantala, Phys. Rev. B **82**, 115106 (2010).
[48] The timing was performed on the Taito supercluster of CSC – IT Center for Science, Finland. Each computing node has Intel Haswell E5-2690v3 processors and the nodes are connected with Infiniband FDR interconnect. For further details of the hardware, see https://research.csc.fi/taito-supercluster (accessed June 1, 2017).
[49] M. E. Casida, in *Recent Advances in Density Functional Methods, Part I*, edited by D. P. Chong (World Scientific, Singapore, 1995), p. 155.
[50] J. P. Perdew, K. Burke, and M. Ernzerhof, Phys. Rev. Lett. **77**, 3865 (1996); **78**, 1396 (1997).
[51] S. Bahn and K. Jacobsen, Comput. Sci. Eng. **4**, 56 (2002).
[52] A. Larsen, J. Mortensen, J. Blomqvist, I. Castelli, R. Christensen, M. Dulak, J. Friis, M. Groves, B. Hammer, C. Hargus, E. Hermes, P. Jennings, P. Jensen, J. Kermode, J. Kitchin, E. Kolsbjerg, J. Kubal, K. Kaasbjerg, S. Lysgaard, J. Maronsson, T. Maxson, T. Olsen, L. Pastewka, A. Peterson, C. Rostgaard, J. Schiøtz, O. Schütt, M. Strange, K. Thygesen, T. Vegge, L. Vilhelmsen, M. Walter, Z. Zeng, and K. W. Jacobsen, J. Phys.: Condens. Matter **29**, 273002 (2017).
[53] See Supplemental Material at http://link.aps.org/supplemental/10.1103/PhysRevB.96.155407 for additional data for all the considered flake sizes.
[54] The monolayer absorption is calculated with GPAW using 16 × 16 k points and a plane-wave basis with a cutoff of 400 eV. The GLLB-SC xc potential is used for ground state and the response is calculated with the random-phase approximation (RPA) [55]. The Lorentzian broadening with FWHM of 190 meV is applied to the monolayer spectrum.
[55] J. Yan, J. J. Mortensen, K. W. Jacobsen, and K. S. Thygesen, Phys. Rev. B **83**, 245122 (2011).
[56] The quadrupole response of Na_{16} in Fig. 4(b) is calculated within the Casida formalism [49] by replacing the dipole matrix elements $\langle i|x|a\rangle$ with $\langle i|x^2|a\rangle$ in the evaluation of the linear response of the KS density matrix.
[57] T. Yasuike, K. Nobusada, and M. Hayashi, Phys. Rev. A **83**, 013201 (2011).
[58] N. Nayyar, V. Turkowski, and T. S. Rahman, Phys. Rev. Lett. **109**, 157404 (2012).
[59] G. W. Bryant, J. Opt. **18**, 074001 (2016).
[60] T. Nagao, S. Yaginuma, T. Inaoka, and T. Sakurai, Phys. Rev. Lett. **97**, 116802 (2006).
[61] U. Krieg, C. Brand, C. Tegenkamp, and H. Pfnür, J. Phys.: Condens. Matter **25**, 014013 (2013).
[62] T. Lichtenstein, J. Aulbach, J. Schäfer, R. Claessen, C. Tegenkamp, and H. Pfnür, Phys. Rev. B **93**, 161408 (2016).
[63] H.-P. Komsa, S. Kurasch, O. Lehtinen, U. Kaiser, and A. V. Krasheninnikov, Phys. Rev. B **88**, 035301 (2013).
[64] O. Lehtinen, H.-P. Komsa, A. Pulkin, M. B. Whitwick, M.-W. Chen, T. Lehnert, M. J. Mohn, O. V. Yazyev, A. Kis, U. Kaiser, and A. V. Krasheninnikov, ACS Nano **9**, 3274 (2015).
[65] M. Gibertini and N. Marzari, Nano Lett. **15**, 6229 (2015).
[66] S. Barja, S. Wickenburg, Z.-F. Liu, Y. Zhang, H. Ryu, M. M. Ugeda, Z. Hussain, Z.-X. Shen, S.-K. Mo, E. Wong, M. B. Salmeron, F. Wang, M. F. Crommie, D. F. Ogletree, J. B. Neaton, and A. Weber-Bargioni, Nat. Phys. **12**, 751 (2016).
[67] S. van der Walt, S. C. Colbert, and G. Varoquaux, Comput. Sci. Eng. **13**, 22 (2011).
[68] J. D. Hunter, Comput. Sci. Eng. **9**, 90 (2007).
[69] W. Humphrey, A. Dalke, and K. Schulten, J. Mol. Graphics **14**, 33 (1996).
[70] J. Stone, An Efficient Library for Parallel Ray Tracing and Animation, Master's thesis, Computer Science Department, University of Missouri-Rolla, 1998.
[71] T. P. Rossi, S. Lehtola, A. Sakko, M. J. Puska, and R. M. Nieminen, J. Chem. Phys. **142**, 094114 (2015).